Effect of solid surface curvature and wall heat loss on the downward flame spread along the edge of thin PMMA sheets

Yuxuan Ma[a,b], Yusuke Konno[a,*], Qiang Wang[a], Longhua Hu[b], Nozomu Hashimoto[a], Osamu Fujita[a]

a Division of Mechanical and Space Engineering, Hokkaido University, Sapporo, 060-8628, Japan

b State Key Laboratory of Fire Science, University of Science and Technology of China, Hefei, Anhui, 230026, China

*Corresponding author: Tel: +81-11-706-6388; Email address: y-konno@eng.hokudai.ac.jp; Postal address: Division of Mechanical and Space Engineering, Hokkaido University, Kitaku, Kita13, Nishi8, Sapporo, Hokkaido 060-8628, Japan.

Abstract

Flames propagating along the sample edges (edge flame) will transform two-dimensional flame spread into three-dimensional flame spread, causing a significant interference with results of material flammability test. A potential method to minimize above effect is utilizing an inert wall to inhibit the side surface of sample with a designed air gap distance. In this work, the downward flame spread along the sample edge with various air gap distances is systematically studied. Cast PMMA with thicknesses from 0.4 to 2.5 mm were used as samples. The general trend of flame spread rate (FSR) at edge with respect to air gap distance can be summarized into three regimes: when the air gap distance is less than 2 mm, the edge flame is quenched by wall heat loss, and the overall flame spread behavior is two-dimensional. Then, the edge flame appears after the air gap distance exceeds 2 mm, resulting in a sharp increase in FSR. This critical air gap distance for the onset of edge flame is less sensitive to the sample thickness. Finally, as the air gap distance continues to increase, the FSR gradually approaches the asymptotic value of the uninhibited sample. With the increase in air gap distance, thermally-thin assumption loses validity as a result of the reduction in residence time of solid phase (larger FSR). To interpret the general trend of FSR with respect to air gap distance, a modified flame spread model based on conventional thermal theory is developed. The effect of air gap distance on flame spread along sample edge is characterized by two correction factors, one of which describes solid surface curvature at sample edge, the other of which is the effective flame temperature considering the heat loss from the spreading flame to the metal wall. The new model well reproduces the experimental results, and further supports the significance of heat loss in the trend of flame spread rate. This work helps to understand the flame spread mechanism under effects of solid surface curvature and heat loss, while also providing scientific support for optimization of material flammability testing standards.

Keywords: Downward flame spread; Edge flame; Air gap distance; Surface curvature; Heat loss.

Nomenclature

A	area	L, l	length
C	coefficient for enhanced flame feedback	Nu	Nusselt number
c	heat capacity	$\dot{q}''$	Flame heat flux
D_Q	quenching diameter	T	Temperature
F, F^*	non-dimensional temperature	t	time
f_e	correction factor for surface curvature	V	velocity
H	heat loss parameter	P	Perimeter
h	heat transfer coefficient	X_F	mass fraction of fuel
Δh_c	heat of combustion		

Greek symbols

α	thermal diffusivity	ρ	density
β	coefficient of thermal expansion	τ	half thickness of sample
δ	thickness/distance	$\tilde{\tau}$	non-dimensional thickness
λ	thermal conductivity		

Subscripts

∞	ambient	p	pyrolysis
air	air gap	pr	preheating zone
e	edge flame	res	residence
eff	effective	s	solid phase
f	flame	w	wall
g	gas phase	x	Sample width direction
ig	ignition	y	Sample thickness direction
$loss$	wall heat loss	z	Flame spread direction

1. Introduction

The necessity for improved fire safety in a space mission stimulates interest in a thorough understanding of material flammability [1, 2]. According to NASA's fire safety standard STD-6001 B [3], the limiting oxygen index (LOI) of a material is recognized as a helpful measure for screening the material fire performance because of its simplicity. The general test device for LOI is now subject to an international standard (ISO 4589) [4, 5], as shown in Fig. 1 (a). The value of the LOI is defined as the minimum oxygen concentration in the oxygen/nitrogen mixture that either maintains flame spread for 180 s or 50 mm of the sample in downward flame spread configuration [4]. If the side surface (the surface with narrow dimension) has negligible effect on the main part of the flame, a typical two-dimensional flame can be obtained. Under this condition, the test phenomena can be interpreted by the thermal properties of samples, based on the classical two-dimensional flame spread theory.

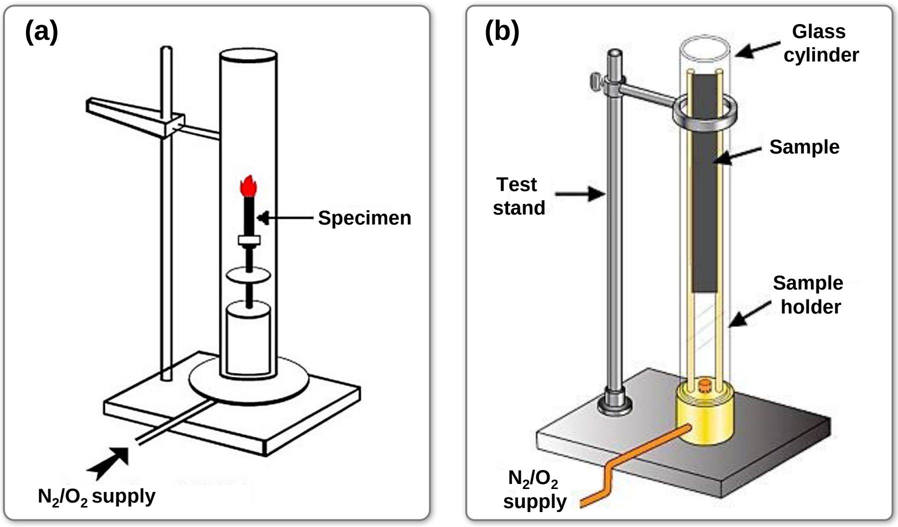

Fig. 1. Schematic of the limiting oxygen index (LOI) test device. (a) General Test configuration [5], and (b) specific test configuration for inhibiting 3-D flame spread with a sample holder [6].

However, in the practical application of LOI tests, the typical dimension of the test sample is 80 to 150 mm long, 10 mm wide, and 4 mm thick [1], the geometrical effect of test sample should not be ignored. Markstein and de Ris [7] reported that the "edge flame" (i.e. the flame propagating along the sample edge) spreads faster than the flame at the centerline of sample, resulting in that the flame front typically forms an inverted V-shape along the sample, and the flame spread behavior becomes three-dimensional. Gong et al. [8] and Zhao et al. [9] also reported that the extra heat supply from the edge flame significantly influences the flame spread process, especially for the thick samples. Additionally, this edge flame effect was also observed in UL-94 tests [10-13], where it resulted in a shorter ignition time, larger flame length and flame spread rate, and maximum local temperatures at the sample edge. Most recently, Delzeit et al. [14] and Matsuoka et al. [15] proposed new flame spread models to predict the flame spread rate along sample edge with various internal angles. The "enhancement of heat flux from flame to solid surface" and "reduction in the heated solid volume" brought on by the solid surface curvature, is the basis of their theoretical analysis.

As the flame extinction is sensitive to the heat transfer process, the formation of edge flame could significantly alter the flammability of a solid material. According to the numerical simulation study by Kumar et al. [16], for PMMA sheets with sides inhibited, the microgravity flame extinguishes at higher oxygen concentration than the flame under normal gravity, however when the sides are permitted to burn, a reversal in this tendency was seen. Experimental study by Comas et al. [17] also identified that the extinction limit can be lower for edge-burning samples in comparison with the inhibited one under normal gravity. In summary, the edge flame effect cannot be overlooked for an uninhibited sample in flammability test.

To prevent the 3-D flame spread over the solid fuel surface, a specific designed sample holder was employed in LOI test, as illustrated in Fig. 1 (b). Nevertheless, this approach still has a fundamental weakness, that the direct contact between the sample and metal sample holder enhances the lateral conductive heat loss in the solid phase. Although stainless steel, which is typically used to make metal sample holders, has a poor thermal conductivity (λ_w~13.8 W/m·K), the flame front over samples with finite width will still display a U-shape because of the lateral conductive heat loss [18-21]. If the thermal conductivity of the test sample is relatively high, the flame extinction limit could be much more sensitive to this lateral heat loss [20-23]. Meanwhile, the effects of conductive heat loss in solid phase on extinction limit are also reported by several literatures on wire fire [24-27] and smoldering combustion [28, 29]. Therefore, minimizing the conductive heat loss in flammability tests of solid materials is of great practical importance.

As indicated in our prior work [19], a compromise technique to quench the edge flame and limit the lateral conductive heat loss from sample to sample holder simultaneously, is to install an inert metal wall (heat sink) at the side surface of the sample with a certain air gap distance. Particularly, the effect of the air gap distance on the flame spread behaviors along the sample edge is of great importance but still poorly understood. In essence, both the wall heat loss (heat loss in the gas phase) and solid surface curvature have an impact on this flame spread configuration. The majority of previous studies on the flame spread under influence of heat loss focused on the heat loss in the solid phase (surface re-radiation and thermal conduction through solid) [23, 30-34], while heat loss in the gas phase received very little attention [31, 35]. This work explores the downward flame spread over thin PMMA sheets of varying sample thickness, while accurately regulating the air gap distance between the side surface of sample and wall. The findings of this work may not only facilitate understanding of the flame spread mechanism with the coupling effect of solid surface curvature and wall heat loss, but it may also serve as a useful reference for more accurately evaluating the flammability of solid materials by LOI test.

2. Experiments

Figure 2 illustrates the experimental design. The cast PMMA sheets (Nitto Jushi Kogyo Co., Ltd.) were used as samples to avoid the significant melting effect on downward flame spread process. The dimensions of PMMA sheet were 40 mm in width, 200 mm in height and 0.4, 0.6, 0.8, 1 and 2.5 mm in thickness (δ_s). PMMA samples were held vertically from the bottom using a vice connected to a perforated plate that was placed horizontally. The effective burning height of sample is 165 mm. Two types of inert metal plates, copper (Cu) and stainless steel (SS), were employed as side walls to inhibit the side surfaces of PMMA sheet. Properties of the materials are presented in Table 1. Dimensions of the inert metal plate were 200 mm in height, 120 mm in width and 4 mm in thickness. The inert metal plates were thick enough to avoid the thermal stress-induced deformation during flame spread process. The inert metal plate was supported vertically by stainless steel section so that the sides of the sample were placed within the thickness of metal plate. The air gap distances (δ_{air}) between inert metal plate and the side surface of PMMA sheet were controlled by vernier calipers (precision: ±0.1 mm). For each test, the air gap distance at two sides of sample were kept same.

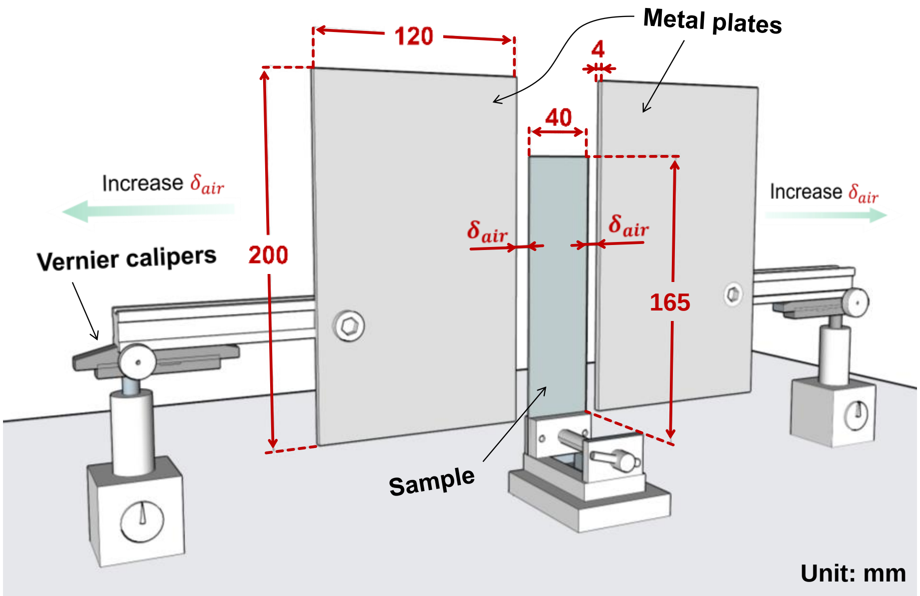

Fig. 2. Experimental apparatus.

Table 1: Properties of PMMA, Cu, SS and gas phase.

Properties	Unit	PMMA [36]	Cu [37]	SS [37]	Gas phase [38]
λ	W/m·K	0.27	398	13.8	0.052
ρ	kg/m^3	1190	8954	8000	0.518
c	J/kg·K	2090	400	384	1183
α	m^2/s	1.09×10^{-7}	1.11×10^{-4}	4.49×10^{-6}	8.48×10^{-5}
T_p	K	647	-	-	-

**The thermal properties of solid phase are evaluated at room temperature (300 K), whereas that of gas phase are evaluated as near 700 K (the characteristic temperature at the leading edge of the flame) [38].*

The ambient conditions for experiments were maintained as 298 K, 101 kPa, and 21% vol. O_2. To ignite the sample uniformly, a lighter flame was manually passed over the top edge of sample until the flame is self-sustained. It only took a few seconds for a thinner sample to ignite, whereas a thicker one required about 20 seconds. The flame spread process was recorded by a digital video camera (29.97 fps) placed in front of the burning sample. The first 20 mm and the last 25 mm of the height of the sample are not included in the measurement, to minimize the ignition effect and ensure enough air entrained from the bottom. The experimental video was analyzed using a Python-based program, called Flame Tracker [39]. The luma tracking method, based on intensity thresholds for each pixel, was employed to identify the pyrolysis front location. The validity of the luma tracking method is demonstrated by a comparison between it and the manual tracking method; more information is provided in Appendix A. For each sample thickness, the test is repeated at least twice (i.e. four sets of FSR data) to minimize uncertainty. Results revealed good reproducibility that the average standard deviation for flame spread rate (FSR) at edge is 3.52%.

3. Experimental results

3.1 Flame spread phenomena

Figure 3 demonstrates the typical time-evolution measurements of pyrolysis front position at edge and centerline of the sample. Pyrolysis front is defined as the boundary between the bubble layers (pyrolysis zone) and the unburned surface, or namely, the boundary between the bright region and dark region over the sample surface as shown in the embedded image of Fig. 3 (a). For steady flame spread, the motion of pyrolysis front can represent the motion of flame front, thus the flame spread rate can be defined through the time evolution of pyrolysis front position.

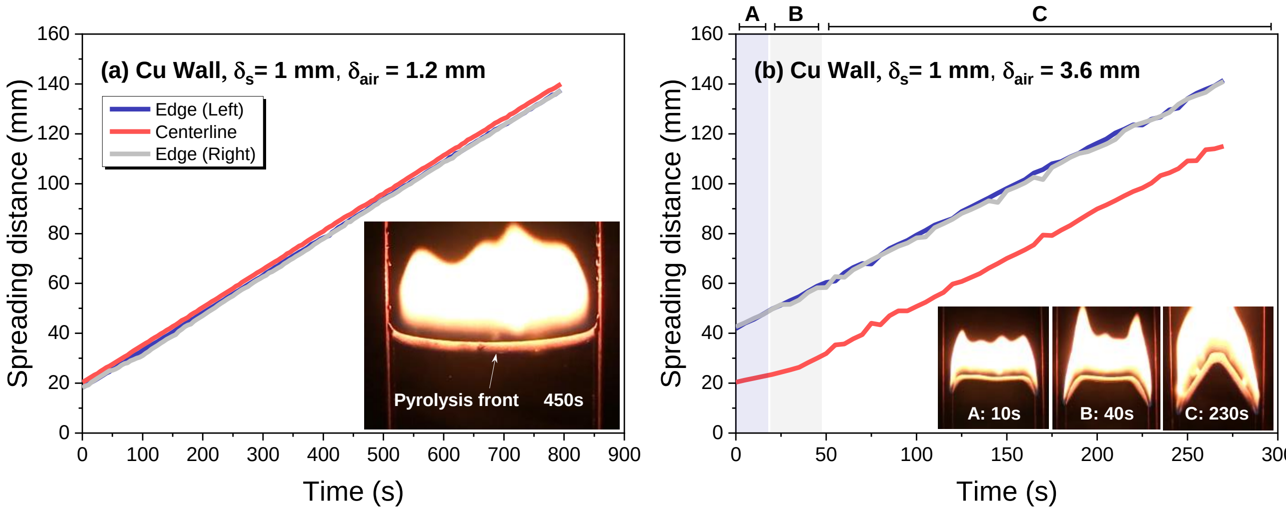

Fig. 3. Typical time evolution of pyrolysis front position at edge and centerline of the sample.

When the air gap distance (δ_{air}) is relatively small, for example δ_{air}=1.2 mm in Fig. 3 (a), the time dependence of pyrolysis front is fairly linear, indicating an approximately constant flame spread rate (FSR). Initially, the FSR at edges is lower than that at centerline caused by the lateral conductive heat loss from the sample to the wall and limited oxygen supply at edge (this stage is not shown in Fig. 3 (a) due to its short duration), therefore the pyrolysis front becomes a U-shape. Nevertheless, the FSRs at edge can rapidly increase to that at centerline driven by the extra heat supply from the curved pyrolysis front. Hence, the steady FSRs for sample with small δ_{air} are less sensitive to the position, and basically are determined by the FSRs at centerline.

As δ_{air} is relatively large (δ_{air}=3.6 mm, Fig. 3 (b)), the pyrolysis front at edge has a reasonably linear time dependency, whereas that at centerline has three typical stages. At initial stage (stage A), the edge flames are stably generated and their spread rates are higher as compared to the 2-D flame spread process (i.e. that at centerline of the sample) due to enhanced heat supply with three-dimensional structure of the edge flames [8, 9, 14, 20]. Because of the non-uniform FSRs along the sample surface, the pyrolysis front formed an inverted U-shape. At transitional stage (stage B), the virgin surface at centerline also started to be affected by the curved pyrolysis front, and the FSR at centerline starts to increase. At developed stage (stage C), the pyrolysis front formed an inverted V-shape, and the flame spread process reached the steady state.

Figure 4 shows the typical flame appearances under different air gap distances (δ_{air}) at developed stage (stage C in Fig. 3 (b)). It is seen that as δ_{air} increases, the pyrolysis front will change from a U-shape to an inverted V-shape. As δ_{air} increases to 1.6 mm and 2 mm, a perfect planar pyrolysis front can be obtained, indicating that lateral conductive heat loss from the solid sample to the wall becomes negligible. However, in these cases, the present flame front is still unable to ignite the fuel-air mixture between the sample side and inert wall due to the considerable wall heat loss. As δ_{air} increases to 2.4 mm, a dim edge flame with an unclear contour is observed, and the pyrolysis front forms an inverted V-shape accordingly. This value of δ_{air} is quite close to quenching diameter (D_Q) for hydrocarbon fuel premixed flames at stoichiometric ratio (2.3 mm for acetylene and 2.5 mm for methane) [36]. Thus, the effect of wall heat loss could dominate the extinction limit of edge flame (i.e. the critical δ_{air} to extinguish edge flame). As δ_{air} continues to increase, the contour of edge flame becomes clearer resulting in increased FSR. Then, the surface area of pyrolysis zone increases, hence releasing more pyrolysis gases and forming a larger flame. The larger flame causes greater air entrainment, which pushes the flame closer to the sample, therefore the flame standoff distance (L_{gy}) at side surface of sample seems slightly decrease with δ_{air}. As the δ_{air} increases to 4 mm, the flame appearance become similar to that of uninhibited sample, indicating that δ_{air} has limited influence on the flame spread process.

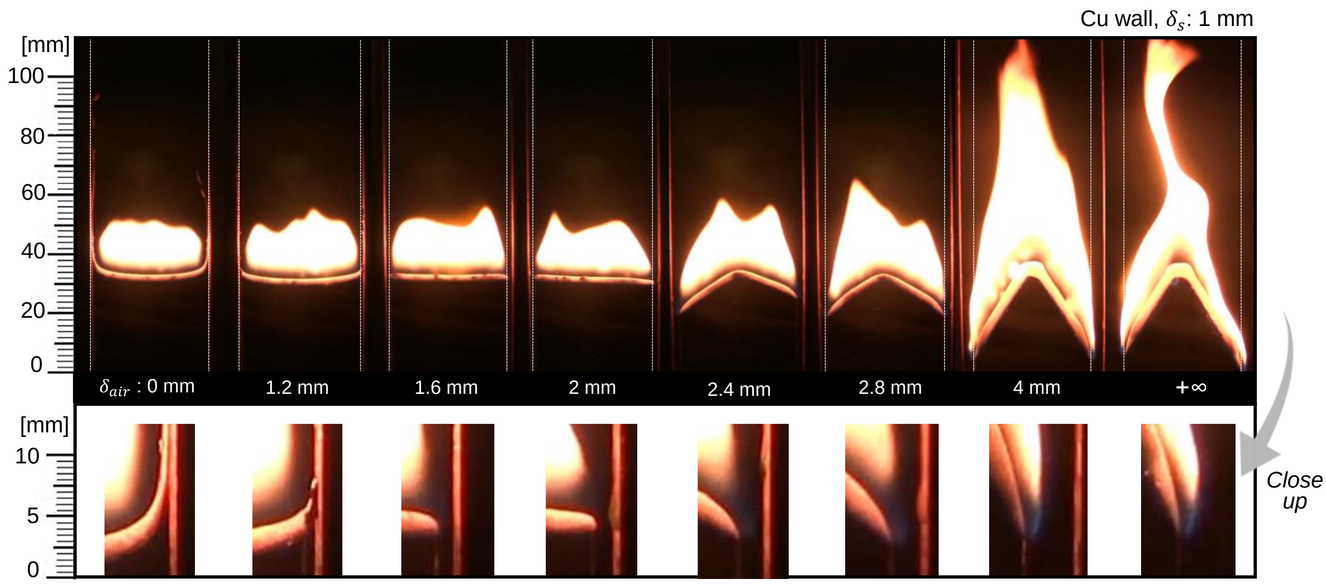

Fig. 4. Snapshots of downward flame spread over PMMA with the sample thickness of 1mm under different air gap distances (δ_{air}). Images at the top are overall flame shape in steady spread region and those at the bottom are the close-up images for the flame at right edge of the sample.

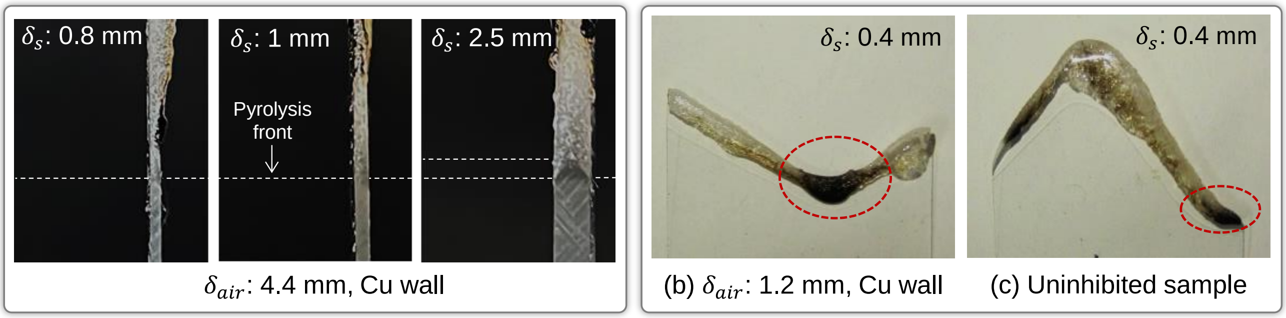

Fig. 5. Typical photographs of the quenched samples. (a) The pyrolysis fronts at the side surface of samples. Surface deformation for 0.4 mm-thick samples (b) inhibited by Cu wall with δ_{air}=1.2 mm and (c) at free burning.

Figure 5 (a) demonstrates the representative images of the pyrolysis front at the sample surface with narrow dimension (side surface). It is seen that the planar pyrolysis front becomes curved as the sample thickness increases. The side surface of the 2.5 mm-thick sample clearly displays an inverted V-shaped pyrolysis front, indicating that the thermal penetration depth along the sample thickness is comparable to the sample's half thickness.

Most of the samples demonstrate the aforementioned phenomenon with the change of δ_{air}. Even though the cast PMMA sheet used here is expected to avoid significant melting, the pronounced surface deformation for 0.4 mm-thickness samples exists as shown in Fig. 5 (b) and (c). The potential reason is that the thin sample is unable to support the hot bubble layer as the surface tension decreases with increasing temperature. These surface deformations usually occur where there is an intensive burning happens, (i.e. at centerline with small δ_{air} and at edge with large δ_{air}), and hence impart extra heat supply to the virgin surface of sample. For these reasons, the pyrolysis front becomes asymmetrical for 0.4 mm-thick samples.

3.2 Flame spread rate (FSR)

Flame spread rate is defined as the first-order derivative of pyrolysis front location versus time. Figure 6 shows the average flame spread rate (FSR) at different locations and stages with the increase in air gap distance. FSRs for 0.4 mm-thick samples show relatively larger uncertainties due to the surface deformation, but the general trend for all the cases is similar. It is concluded that the FSR at centerline in initial stage (stage A in Fig. 3 (b)) are independent of the air gap distance (δ_{air}), and the FSRs in developed stages (stage C in Fig. 3 (b)) are less sensitive to the locations. For the samples inhibited by Cu wall, because the edge flame is quenched by wall, the developed FSRs keep almost constant when δ_{air} is less than 2 mm, and the overall flame spread process is controlled by the FSR at centerline (2-D flame spread). In these cases, the pyrolysis front shows a U-shape curved as indicated in Fig. 4, revealing that the lateral conductive heat loss from solid sample to wall exists. However, this heat loss is too weak to affect flame spread process due to the poor thermal conductivity of PMMA. When δ_{air} exceeds 2 mm, the developed FSRs will increase rapidly with δ_{air}, and controlled by the FSRs at edge (3-D flame spread). As δ_{air} increases above a critical value, the side wall effect becomes weak and the developed FSRs seem less sensitive to δ_{air} accordingly. The critical air gap was found to be around 3.6 mm for 0.4 mm, 0.6 mm, and 0.8 mm thick samples, and around 4 mm and 4.4 mm for 1 mm and 2.5 mm thick samples, respectively.

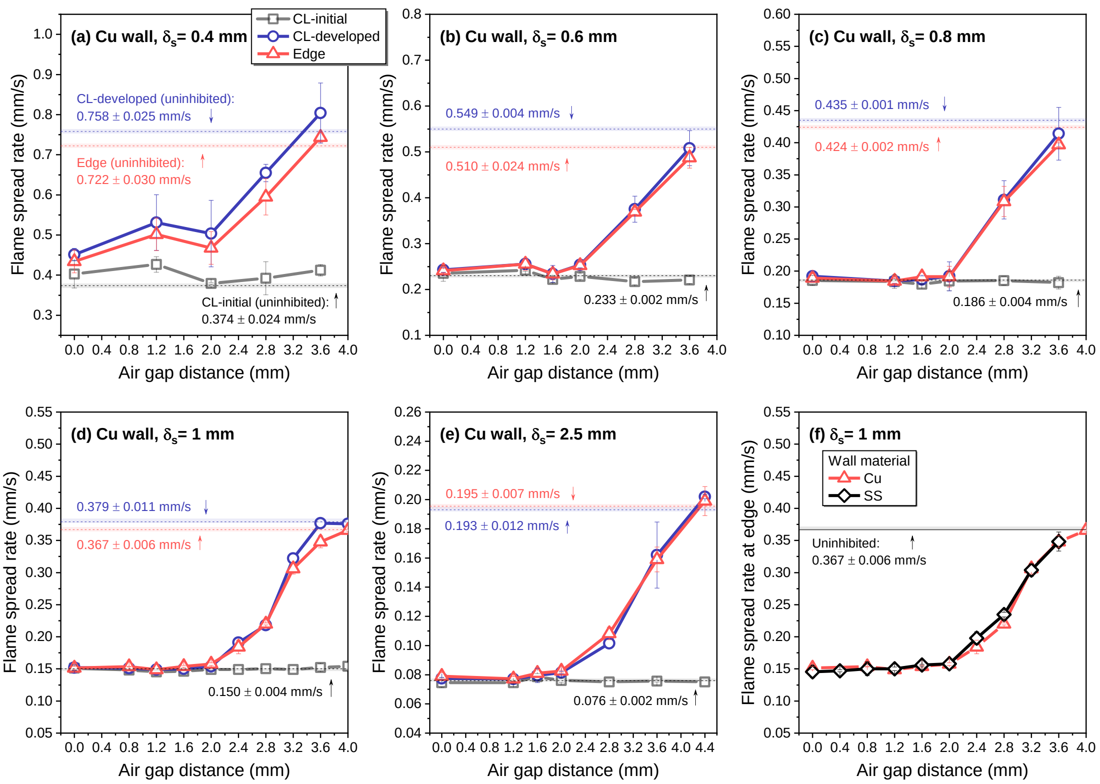

Fig. 6. Variation of flame spread rate at edge and centerline (CL) of the sample with air gap distance.

In normal gravity, the effective buoyant flow velocity ($V_{g,eff}$), i.e. the local flow velocity seen by flame front considering the boundary layer effect, is significantly larger than the flame spread rate (V_f) [18], hence it is assumed that the opposing flow velocity relative to flame ($V_r = V_{g,eff} + V_f$) is equal to $V_{g,eff}$. Thus, the conductive heat loss from the flame to the wall, which is proportional to the flow residence time $t_{g,res} \approx \alpha_g/V_r^2 \approx \alpha_g/V_{g,eff}^2$, is anticipated to be irrespective of sample thickness, even though V_f changes with sample thickness. It is consistent to the experimental result that the inflection point where the developed FSRs start to increase with δ_{air} (around 2 mm), i.e. the extinction limit of edge flame, are is less sensitive to sample thickness. Because the wall heat loss is inversely proportional to the distance between wall and flame, thus it is expected that the δ_{air} at flame extinction limit may be very close to the flame standoff distance (L_{gy}). For simplicity, L_{gy} is assumed to be 2 mm, yielding $V_{g,eff} \approx \alpha_g/L_{gz} \approx \alpha_g/L_{gy}$ ≈4.2 cm/s with the value of α_g in Table 1. This value of $V_{g,eff}$ is slightly larger than that for 2-D flame spread (~1.9 cm/s [18]), but is still lower than the characteristic buoyant flow velocity under natural convection $V_{g,NC} \approx \left(\alpha_g g\beta\Delta T\right)^{1/3}$ ≈12.9 cm/s ($\beta \approx 1/T_p$, $\Delta T \approx T_{f,ad} - T_{\infty}$, $T_{f,ad}$ = 2308 K is the adiabatic flame temperature) [35]. It is possibly because the boundary layer thickness is thinner for surface with curvature as compared to a flat surface [40], and hence the effective flow velocity at flame front becomes larger.

The effect of side wall material is investigated, as shown in Fig. 6 (f). However, the FSRs at the edge are less sensitive to the side wall material, despite that the ratio of thermal conductivities between Cu and SS is as high as 28.8 (Table 1). The temperature measurement indicates that there is only around 10 K of difference between the side surface temperatures of these two walls at flame front, due to the large thermal capacity of the 4 mm-thick walls. Details of the temperature measurement of wall can be found in Appendix B. Consequently, the effect of side wall material in this work could be negligible.

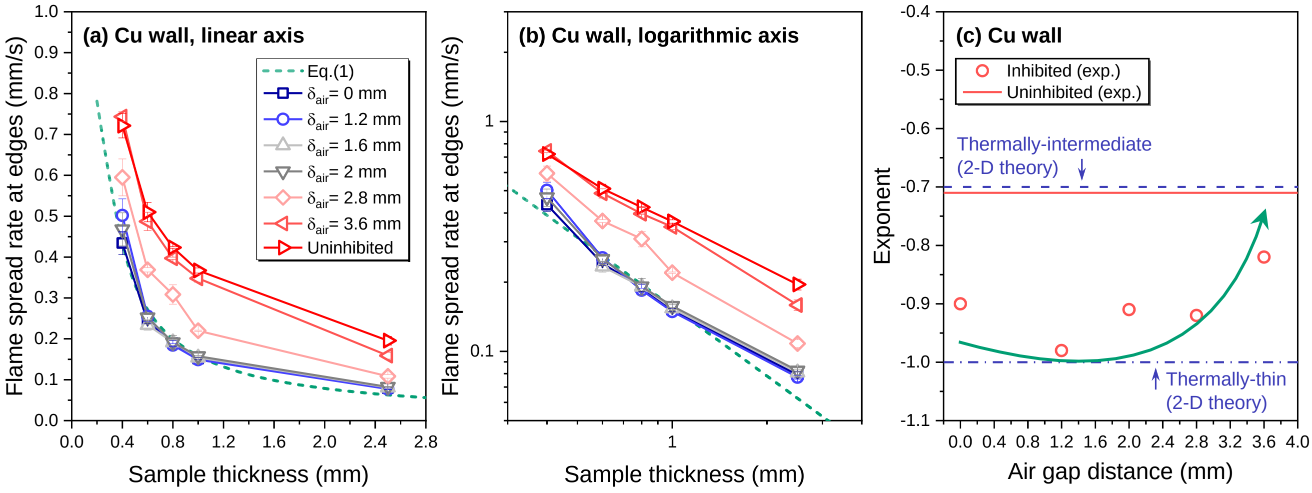

Fig. 7. Flame spread rate at edge variation with sample thickness in (a) linear axis, and (b) logarithmic axis. (c) The best fitting exponent *n* as a function of air gap distance from $V_f \propto {\delta_s}^n$.

Figure 7 (a) shows the variation of FSR at edge with sample thickness (δ_s) in linear axis. It is seen that, for the cases without edge flame ($\delta_{air} \leqslant 2$ mm), the FSR at edge significantly decreases with sample thickness at initial, then decreases more mildly, indicating that it is approaching the thermally-thick limit. However, for cases with edge flame ($\delta_{air} > 2$ mm), FSR at edges still decreases sharply when the sample thickness approaches 2.5 mm, revealing that the heated solid volume is still sensitive to the sample thickness. If the same data are plotted in logarithmic axis, fairly linear trend indicates that the FSR at edges can be expressed as $V_f \propto {\delta_s}^n$. Figure 7 (c) shows the best fitting exponent *n* as a function of air gap distance from $V_f \propto {\delta_s}^n$. Experimental results show that *n* varies between -1 and -0.9 when $\delta_{air} < 2.8$ mm, which is close to the exact solution for the two dimensional flame spread rate over thermally thin material given by Delichatsios [41]:

$$V_{f,thn} = \frac{\pi}{4} \frac{\lambda_g}{\rho_s c_s \tau} F \, , \tag{1}$$

where $F = \frac{T_f - T_p}{T_p - T_\infty} \approx 4.76$ [18], and $\tau = \delta_s/2$. As shown in the dash line in Fig. 7, Eq. (1) predicts the FSR without edge flame ($\delta_{air} \leqslant 2$ mm) quite well. Meanwhile, it is seen that *n* lies between -0.9 to -1 when $\delta_{air} \leqslant 2.8$ mm, then increases sharply with the increasing δ_{air}, and finally approach an asymptotic value of -0.71 for the uninhibited sample. This asymptotic value is quite close to the value for the thermally-intermediate flat fuel (-0.7) as reported in [42]. The thermal penetration depth (τ_h) below the sample surface can be estimated as [18, 42]:

$$\tau_h \approx \sqrt{\alpha_s t_{s,res}} = \sqrt{\alpha_s \frac{L_{gz}}{V_f}} \approx \sqrt{\frac{\alpha_s \alpha_g}{V_{g,eff} V_f}}, \tag{2}$$

where $t_{s,res}$ is the residence time in solid phase, L_{gz} is the gas phase thermal diffusion length. Using the physical properties in Table 1, the ratio of half thickness of the sample (τ) to τ_h, $\tilde{\tau} = \tau/\tau_h$, can be obtained. For 2-D flame spread ($\delta_{air} \leq 2$ mm), $\tilde{\tau}$ is lower than 0.52, indicating that the sample is considered to be thermally thin ($\tilde{\tau}$<0.6) [42]. However, in the cases with edge flame (δ_{air}>2 mm), the residence time in solid phase decreases, resulting in the reduction of thermal penetration depth. In this work, maximum $\tilde{\tau}$ for uninhibited sample could be as high as 1.2, revealing that the sample is regarded as thermally intermediate (0.6<$\tilde{\tau}$<2) [42]. Furthermore, unlike 2-D flame spread, the thermal penetration depth for 3-D flame spread is somewhat more complex as a function of τ because of mutual interface at the sample edge. Namely, the thermally-thick limit for solid fuel can be altered due to the surface curvature of solid fuel. Similar phenomenon is also reported in [43], which identified that the thermally-thick limit occurs for a PMMA cylinder with the radius of 1.2 mm, while that of a flat fuel occurs at τ of about 5 mm, because the surface curvature causes increase in FSR due to enhancement of the heat flux from the flame to the solid surface.

4. Modelling of flame spread along sample edge inhibited by wall

As discussed above, there are two main aspects to the impact of air gap distance (δ_{air}) on the flame spread along sample edge. The first is an enhancement of heat flux from the flame to the solid surface and a modification in heated solid volume caused by surface curvature, and the second is the reduction of edge flame temperature under small δ_{air} due to significant conductive heat loss from the flame to the wall. Therefore, the following theoretical analysis attempts to consider these two effects into two correction factors, in order to modify the two-dimensional fire spread expression based on classical thermal theory. For simplicity, the following analysis assumes that the sample width is infinite, the Damköhler number is infinite, and the radiative heat flux is ignored.

4.1 Surface curvature effect

The increase in heat flux from the flame to the solid surface and the reduction in heated solid volume are the dominant reason for the increasing flame spread rate over curved solid surface [40, 43, 44]. Based on these understandings, previous works [14, 15] have been modeled the effect of solid surface curvature on the flame spread rate by developing a dimensionless number that modifies the flame spread rate itself. In this work, a different approach is developed to evaluate the effect of solid surface curvature on the flame spread rate using the energy conservation law.

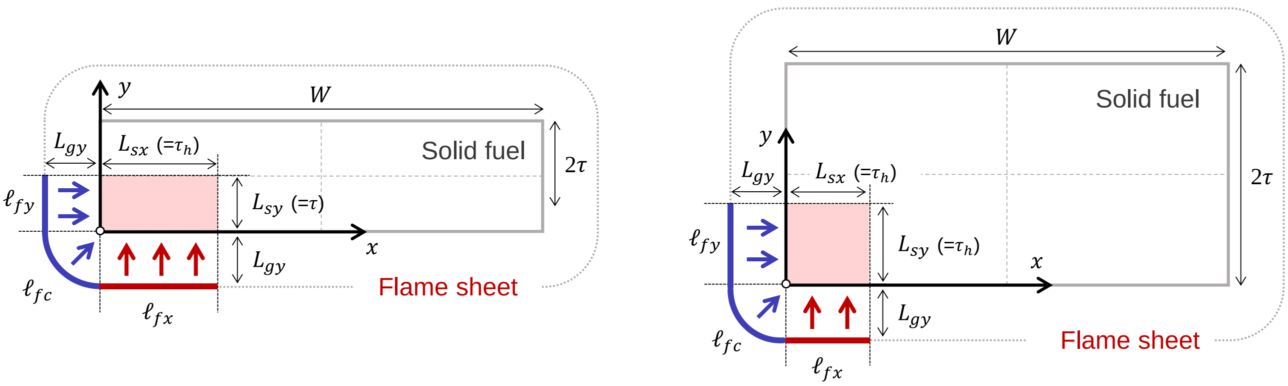

Fig. 8. Geometrical relationship of the flame to the sample surface at edges (top view). For thermally-thin, $\tau \leq \tau_h$; for thermally-thick, $\tau > \tau_h$.

Figure 8 is a top view showing the geometrical relationship between the flame surface of the spreading flame and the cross-section of the solid fuel. In this figure, thermally-thin and thermally-thick are categorized by the relative magnitudes between half thickness of sample (τ) and thermal penetration below the sample surface (τ_h), or namely, for thermally-thin, $\tau \leq \tau_h$; for thermally-thick, $\tau > \tau_h$. The cross-sectional area ($A_{pr,s}$) and effective perimeter ($P_{pr,s}$) of controlled volume in solid phase are defined as $A_{pr,s} = L_{sx}L_{sy}$ and $P_{pr,s} = L_{sx} + L_{sy}$, respectively. Here, the thermal penetration depth along sample thickness (L_{sy}) and that along sample width (L_{sx}) are given as:

$$L_{sx} = \min[W/2\,, \tau_h] = \tau_h\,, \tag{3}$$

$$L_{sy} = \min[\tau, \tau_h]\,. \tag{4}$$

τ_h can be estimated from Eq. (2). It is seen that the heated solid volume is also controlled by the thermal penetration depth along sample width even for thermally-thin case.

A modified energy balance equation of solid phase in preheating zone is formulated as:

$$V_{f,e}\rho_s c_s A_{pr,s}\left(T_p - T_\infty\right) = \frac{\pi}{4} P_{pr,s} L_{gz} \dot{q}''_{in}\,, \tag{5}$$

where $V_{f,e}$ is the flame spread rate along the sample edge, L_{gz} is the gas phase preheating length, π/4 is a correction factor considering the realistic heat flux profile near flame front [41], $\dot{q}''_{in}$ is the heat flux from flame to the solid surface, given as:

$$\dot{q}''_{in} = C\lambda_g\left(T_f - T_p\right)/L_{gy}\,. \tag{6}$$

In Eq. (6), L_{gy} is the standoff distance of spreading flame, C is the enhanced flame heat flux coefficient caused by surface curvature, and hence $C \geqslant 1$ should be fulfilled. Strictly speaking, C is a function of the equivalent radius of the controlled volume in solid phase [40, 43, 44], for instance, C decreases as radius increases and finally approach unity (flat surface). Nevertheless, according to the experimental results reported in [14], flame spread rate along the edge is strongly related to the internal angel of corner, rather than the aspect ratio (or cross-section area) of sample, indicating that C is dominated by the internal angel. Herein, for the sake of brevity, C is assumed to be a constant.

Solving Eqs. (5) and (6) for the flame spread rate, one obtains:

$$V_{f,e} = f_e V_{f,thn} \,, \tag{7}$$

where, $V_{f,thn}$ is the 2-D flame spread expression given by Eq. (1), and f_e is a correction factor for surface curvature, expressed as:

$$f_e = C\frac{L_{gz}}{L_{gy}} \cdot \frac{\left(L_{sx} + L_{sy}\right)\tau}{L_{sx}L_{sy}} \approx \begin{cases} C\left(1 + \dfrac{\tau}{\tau_h}\right), \tau_h \geq \tau \\ 2C\dfrac{\tau}{\tau_h} \quad , \tau_h < \tau \end{cases} . \tag{8}$$

It is seen that the effect of solid surface curvature at sample edge can be reduced into a correction factor (f_e). Because the conductive heat loss in the solid phase is considered in the energy balance, energy balance equation becomes a nonlinear function of flame spread rate, or namely, in Eq. (7), $V_{f,E}$ is also incorporated in f_e implicitly. With appropriate C, Eqs. (7) and (8) can be used to predict the flame spread at edge without wall heat loss. As shown in Fig. 9, this model well reproduces the experimental results with C=1.4, where the experimental f_e is calculated by the ratio of FSR for uninhibited sample to 2-D FSR (Eq. (1)). Noted that the present model may somehow underestimate f_e for 2.5 mm-thick sample. As shown in Figs. 5 (a) and 7, it is probably resulted from that 2.5 mm-thick sample could be regarded as thermally-intermediate along y-axial, thus the experimental f_e for 2.5 mm-thick sample lies between thermally-thin branch and thermally-thick branch.

The increase in flame spread rate over edges compared to that over flat surfaces can be interpreted by the energy balance equation (Eq. 5) in preheating zone. The flame spread rate can be rewritten as $V_{f,e} = L_{gz}/t_{ig,e}$, where $t_{ig,e}$ denotes the ignition time ($t_{ig,e}$), in other words, the heating time for the solid surface to reach the pyrolysis temperature. Therefore, the increase in flame spread rate can be associated with the decrease in ignition time of unburned solid surface. Substituting the Eqs. (3), (4), and (6) into $V_{f,e} = L_{gz}/t_{ig,e}$, it yields: if $\tau_h \geq \tau$, $t_{ig,e} \approx \frac{t_{ig,thn}}{C(1+\tau/\tau_h)} = \frac{1}{C(1+\tau/\tau_h)} \cdot \frac{4L_{gy}\rho_s c_s \tau}{\pi \lambda_g F}$; if $\tau_h < \tau$,

$t_{ig,e} \approx \frac{t_{ig,thk}}{2C} = \frac{1}{2C} \cdot \frac{4L_{gy}\rho_s c_s \tau_h}{\pi \lambda_g F}$, where $t_{ig,thn}$ and $t_{ig,thk}$ are the ignition time for the thermally-thin and thermally-thick flat surface, respectively. It indicates that the decrease in ignition time at edges is attributed to the coupling effect of the increased heat supply from flame (C=1.4) and the reduction in the heated volume. It is consistent with the mechanism of increased flame spread rate over cylindrical surface [40, 43, 44].

The sample width also plays important role in the opposed flame spread under suppressed natural convection [45] and the concurrent flame spread [46]. However, for opposed flame spread under natural convection, this effect only becomes important when the sample width approaches the sample thickness [47]. In the above case, the thermal penetration depth along sample width is $L_{sx} = \min[W/2, \tau_h]$, hence the final expression of Eq. (8) will be altered. An interesting further work is to further check the validity of the proposed model for the samples with various widths.

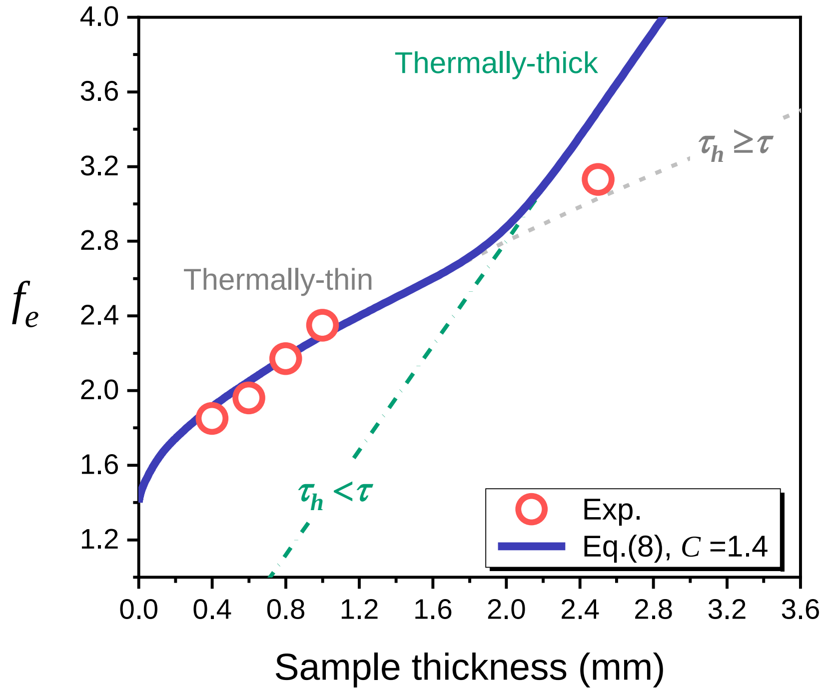

Fig. 9. Comparison of experimental results for curvature correction factor (f_e) and theoretical prediction based on Eq. (8). The experimental f_e is calculated by the ratio of FSR for uninhibited sample to 2-D FSR (Eq. (1)). The dash line and dot dash line denote the extensions of thermally-thin branch ($\tau_h \geq \tau$) and thermally-thick branch ($\tau_h < \tau$), respectively.

4.2 Wall heat loss effect

In preheating zone, the temperature gradient between the flame and side wall will increase significantly as the air gap distance (δ_{air}) decreases. Therefore, it is expected that the temperature of edge flame ($\ell_{fy} + \ell_{fc}$) will drop because of the considerable heat loss from the gas phase to the metal wall. If the flame temperature falls below a critical value, the edge flame will be quenched.

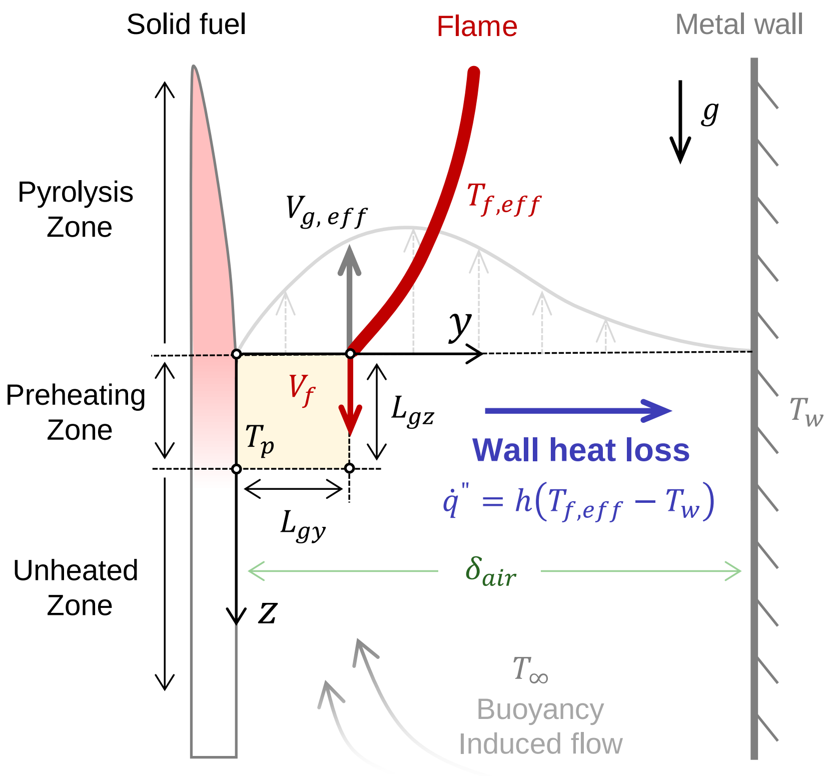

Fig. 10. Schematic of downward flame spread over a solid fuel with heat loss from gas phase.

The schematic of downward flame spread over a solid fuel with wall heat loss under natural convention is shown in Fig. 10. Assuming that the heat transfer between the combustible gaseous mixture and side wall is the main source of heat loss, and $L_{gz} \approx L_{gy} \approx \alpha_g/V_{g,eff}$, the energy balance equation in the gas phase preheating zone is formulated as:

$$\rho_g X_F \Delta h_c V_r - h(T_{f,eff} - T_w) = (T_{f,eff} - T_\infty) c_g \rho_g V_r \,, \qquad (9)$$

where X_F is the mass fraction of fuel, Δh_c is the heat of combustion, h is the heat transfer coefficient between the combustible gaseous mixture and the side wall, $T_{f,eff}$ is the effective flame temperature with wall heat loss, T_w is the side wall temperature, $V_r = V_{g,eff} + V_f \approx V_{g,eff}$ is the opposing flow velocity relative to flame under natural convection. The LHS and RHS of Eq. (9) denote the net heat release rate and the enthalpy change rate of gas phase, respectively. Therefore, the explicit expression of $T_{f,eff}$ can be solved from Eq. (9):

$$T_{f,eff} = T_\infty + \frac{1}{1+H}\left[\frac{X_F \Delta h_c}{c_g} - H(T_\infty - T_w)\right] . \tag{10}$$

The heat loss parameter H is expressed as:

$$H = \frac{h}{c_g \rho_g V_{g,eff}} . \tag{11}$$

It is seen that H represents the ratio of heat loss through the wall to the heat conduction in preheating zone. H is proportional to h, but decreases with the increase in $V_{g,eff}$ due to the reduction of flow residence time. Furthermore, it is seen that the wall heat loss will be suppressed if the wall temperature (T_w) is higher than the ambient temperature (T_∞). Also, the term $H(T_\infty - T_w)$ can be neglected if T_w is the same as T_∞.

If the heat loss is negligible (h = 0), the adiabatic flame temperature is derived from Eq. (10) as:

$$T_{f,ad} = \frac{X_F \Delta h_c}{c_g} + T_\infty . \tag{12}$$

It is seen that $T_{f,ad}$ is determined by the thermodynamic parameters, and is independent of $V_{g,eff}$ (or namely, the flow residence time). Previous literature [18] reported that $T_{f,ad} - T_p = F\left(T_p - T_\infty\right)$ could reproduce the experimental 2-D FSR over PMMA when F=4.76 is satisfied, thus it yields $T_{f,ad}$=2308 K.

If the wall heat loss effect is significant ($h \neq 0$) when the wall approaches to the solid fuel, $T_{f,eff}$ can be given in terms of $T_{f,ad}$ from Eqs. (10) and (12), as:

$$T_{f,eff} = T_\infty + \frac{1}{1+H}\left[T_{f,ad} - T_\infty - H(T_\infty - T_w)\right]. \tag{13}$$

As indicated in Appendix, the temperature increase of wall at flame front could be negligible. Here, let T_w is equal to T_∞, it yields:

$$T_{f,eff} = T_\infty + \frac{1}{1+H}\left(T_{f,ad} - T_\infty\right). \tag{14}$$

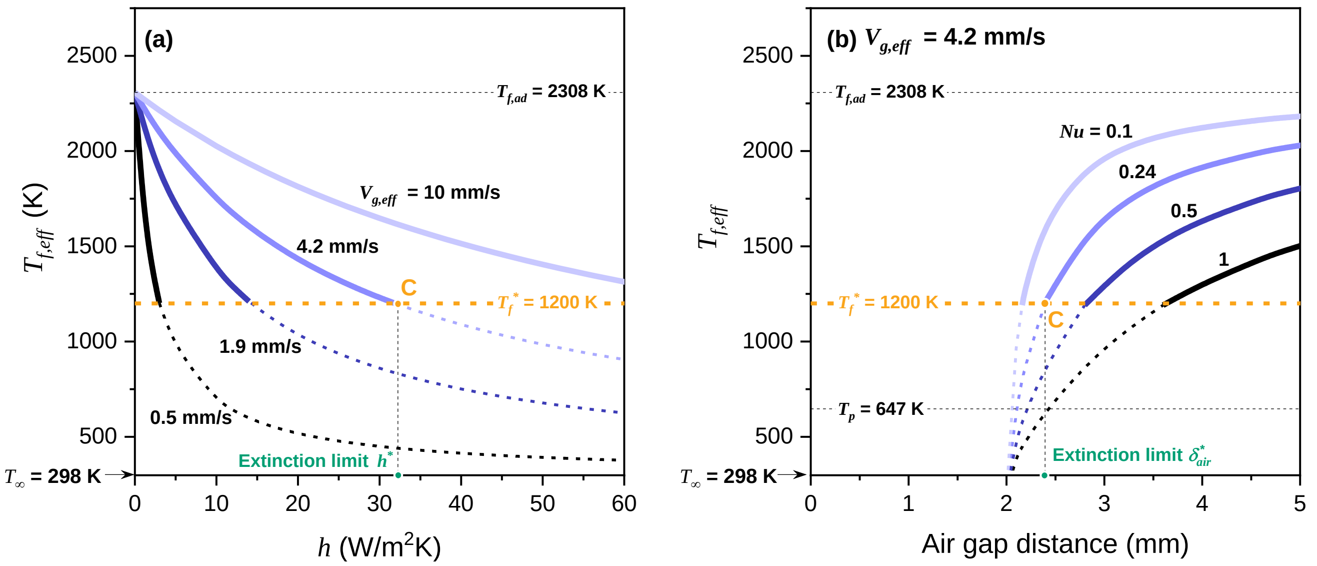

Fig. 11. (a) Effective flame temperature ($T_{f,eff}$) as a function of the heat transfer coefficient between the flame and the side wall (h) with different effective flow velocity ($V_{g,eff}$). $T_{f,eff}$ is calculated from Eq. (14) with properties in Table. 1, $T_{f,ad}$=2308 K and T_∞=298 K. (b) $T_{f,eff}$ vs. δ_{air} with different Nusselt number. $T_{f,eff}$ is calculated from Eqs. (14) and (16) with $V_{g,eff}$=4.2 cm/s.

Figure 11(a) demonstrates the variation of $T_{f,eff}$ with respect to h calculated from Eq. (14). Four effective flow velocities ($V_{g,eff}$: 0.5, 1.9, 4.2 and 10 cm/s) are presented as typical calculation results. As h increases from zero, $T_{f,eff}$ decreases rapidly from $T_{f,ad}$ at initial, then decreases more mildly, and finally approaches an asymptotic value of T_∞. Noted that, at lower temperatures, chemical reaction time becomes too large as compared to flow residence time, and further slows the chemical reaction rate. This causes a negative feedback in the system, and eventually the flame will be quenched. For the diffusion flame over PMMA, the empirical temperature under this limiting condition (T_f^*) is around 1200 K [48]. The monotonically decreasing $T_{f,eff}$ has one point of intersection with $y = T_f^*$, point C. The critical heat transfer coefficient h^* corresponding to point C represents the extinction limit of edge flame. h^* can be derived from Eq. (14) by replacing $T_{f,eff}$ with T_f^*, expressing as:

$$h^* = c_g \rho_g V_{g,eff} \left(\frac{T_{f,ad} - T_\infty}{T_f^* - T_\infty} - 1 \right) . \tag{15}$$

It is seen that h^* is proportional to $V_{g,eff}$, because of shorter flow residence time. Moreover, when the edge flame could sustain ($h < h^*$), $T_{f,eff}$ decreases more rapidly as $V_{g,eff}$ decreases, indicating that flame spread behavior will be more sensitive to heat loss under low flow velocity conditions, for instance, under microgravity. Under natural convection, $V_{g,eff}$ can scale with flame temperature as $V_{g,eff} \sim V_{g,NC} \approx \left(\alpha_g g \beta \Delta T\right)^{1/3}$ by equating the buoyancy term to inertial term in the momentum equation at flame front. However, the flow field around edge flame is also influenced by the main part of the flame, which is not be cooled by the side wall. Given the approximate nature of this analysis, the effective flow imposed to edge flame is assumed to be a constant (4.2 cm/s) in the following discussion. This value of $V_{g,eff}$ is obtained when the flame standoff distance (L_{gy}) is set as 2 mm, as discussed in section 3.2.

For the edge flame inhibited by side wall, it is noted the similarity of present configuration with the premixed flame propagation between two parallel walls. Thus, it yields:

$$Nu = \frac{h\left(\delta_{air} - L_{gy}\right)}{\lambda_g} . \tag{16}$$

The relative importance of wall heat loss is characterized by the heat loss parameter (H) as indicated in Eq. (11). Substituting Eq. (16) into Eq. (11), it yields $H = \frac{Nu}{\delta_{air}/L_{gy} - 1}$. It reveals that the magnitude of wall heat loss is determined by two length scales, L_{gy} and δ_{air}. Wall heat loss diverges to infinity as δ_{air} approaches the same magnitude as L_{gy}. It is the physical basis for the assumption that $\delta_{air,c}^*/L_{gy} = 1$, where $\delta_{air,c}^*$=2 mm is the critical air gap distance for the onset of edge flame.

Substituting Eq. (16) into Eq. (14), $T_{f,eff}$ can be correlated with δ_{air}. Figure 11 (b) demonstrates the variation of $T_{f,eff}$ with respect to h calculated from Eqs. (14) and (16). Four Nusselt number (Nu: 0.1, 0.24, 0.5 and 1) are presented as typical calculation results. It is seen that $T_{f,eff}$ decreases monotonically with decreasing δ_{air}, and drops significantly as approaching $\delta_{air} = L_{gy}$ (2 mm). The variation of $T_{f,eff}$ with δ_{air} shows a similar trend to flame spread rate, indicating that wall heat loss might be dominant in controlling the trend of flame spread rate. Meanwhile, $T_{f,eff}$ increases with decreasing Nu, and at low Nu, $T_{f,eff}$ is more sensitive to δ_{air} near $\delta_{air} = L_{gy}$. In the present work, the value of Nu is given to satisfy the experimental FSR at δ_{air}=2.8 mm for 0.8 mm-thick sample (the predictive model for FSR will elaborate in section 4.3), thus it yields Nu=0.24. It is seen that the edge flame will be quenched near δ_{air}=2.4 mm, which is consistent with the experimental result as shown in Fig. 4.

4.3 Comparison with experimental results

The analysis begins with the assumption that only the flame at the side surface ($\ell_{fy} + \ell_{fc}$) will be cooled by the metal wall, while the rest of the flame (ℓ_{fx}) remains at $T_{f,ad}$, as shown in Fig. 8. Substituting Eq. (8) into Eq. (6), the equivalent flame heat flux imposed to controlled volume ($\dot{q}''_{in}$) without wall heat loss can be expressed in terms of f_e, as:

$$\dot{q}''_{in} = \frac{f_e L_{sx} L_{sy}}{\left(L_{sx} + L_{sy}\right)\tau} \cdot \lambda_g \frac{T_f - T_p}{L_{gy}} \ . \tag{17}$$

If the heat flux from ℓ_{fx} to L_{sx} takes the same form as a 2-D flame spread, i.e. $\dot{q}''_{in,x} = \lambda_g \frac{T_f - T_p}{L_{gy}}$, the flame heat flux to the side surface of sample (from $\ell_{fy} + \ell_{fc}$ to L_{sy}) considering curvature effect is:

$$\dot{q}''_{in,y} L_{sy} = P_{pr,s} \dot{q}''_{in} - \dot{q}''_{in,x} L_{sx}$$
$$\Rightarrow \dot{q}''_{in,y} = \lambda_g \left(f_e \frac{L_{sx}}{\tau} - \frac{L_{sx}}{L_{sy}} \right) \frac{T_f - T_p}{L_{gy}} \ . \tag{18}$$

Through this approach, the effect of flame temperature at the side surface ($\ell_{fy} + \ell_{fc}$) is extracted, thus the wall heat loss effect can be incorporated by replacing T_f with $T_{f,eff}$ in Eq. (18).

Based on these, the modified energy balance equation incorporating wall heat loss and solid surface curvature is formulated as:

$$V_{f,e,loss}\rho_s c_s A_{pr,s}\left(T_p - T_\infty\right) = \frac{\pi}{4} L_{gz}\left(\dot{q}''_{in,y} L_{sy} + \dot{q}''_{in,x} L_{sx}\right), \tag{19}$$

where $V_{f,e,loss}$ is the flame spread rate along the sample edge with wall heat loss, $A_{pr,s} = L_{sx}L_{sy}$, $\dot{q}''_{in,y}$ is estimated from Eq. (18) by replacing T_f with $T_{f,eff}$ from Eq. (14), $\dot{q}''_{in,x} = \lambda_g \frac{T_{f,ab}-T_p}{L_{gy}}$, π/4 is a correction coefficient [41]. Assuming $L_{gx} \approx L_{gy} \approx L_{gz} \approx \alpha_g / V_{g,eff}$, Eq. (19) can be rewritten as:

$$V_{f,e,loss} = \frac{\pi}{4} \frac{\lambda_g}{\rho_s c_s \tau} F^*, \tag{20}$$

where,

$$F^* = \frac{\tau}{L_{sy}} F + \left(f_e - \frac{\tau}{L_{sy}}\right) \frac{T_{f,eff} - T_p}{T_p - T_\infty} = \begin{cases} F + (f_e - 1)\dfrac{T_{f,eff} - T_p}{T_p - T_\infty} & ,\tau_h \geq \tau \\ \dfrac{\tau}{\tau_h} F + \left(f_e - \dfrac{\tau}{\tau_h}\right)\dfrac{T_{f,eff} - T_p}{T_p - T_\infty} & ,\tau_h < \tau \end{cases}. \tag{21}$$

Figure 12 compares the experimental results with theoretical predictions based on Eq. (20). Two correction factors, f_e and $T_{f,eff}$, are solved from Eqs. (8) and (14), respectively. It is seen that the new model can well reproduce the experimental results, revealing that the present analysis could capture the dominant mechanism of flame spread inhibited by wall. Although the edge flame will be quenched when δ_{air} is lower than 2.4 mm, the slow exothermic oxidation reaction still exists in the gaseous combustible mixture. Therefore, the flame spread rates are expected to be larger than 2-D FSR in a narrow region near flame extinction limit (h^*). For instance, experimental FSRs are still larger than 2-D FSR when 2 mm<δ_{air}<2.4 mm. The proposed model slightly overestimates the FSR in this region, possibly due to the neglect of chemical time under small Da number. If the temperature of gaseous combustible mixture is lower than T_p as δ_{air} continues decreases, the heat flux to the side surface of sample (from $\ell_{fy} + \ell_{fc}$ to L_{sy}) becomes negative. Therefore, FSR along the edge will be lower than that at centerline, and the pyrolysis front becomes a "U" shape. Eventually, the overall flame spread is controlled by the flame at centerline, where the basic simplifications in the present analysis may not be applicable anymore.

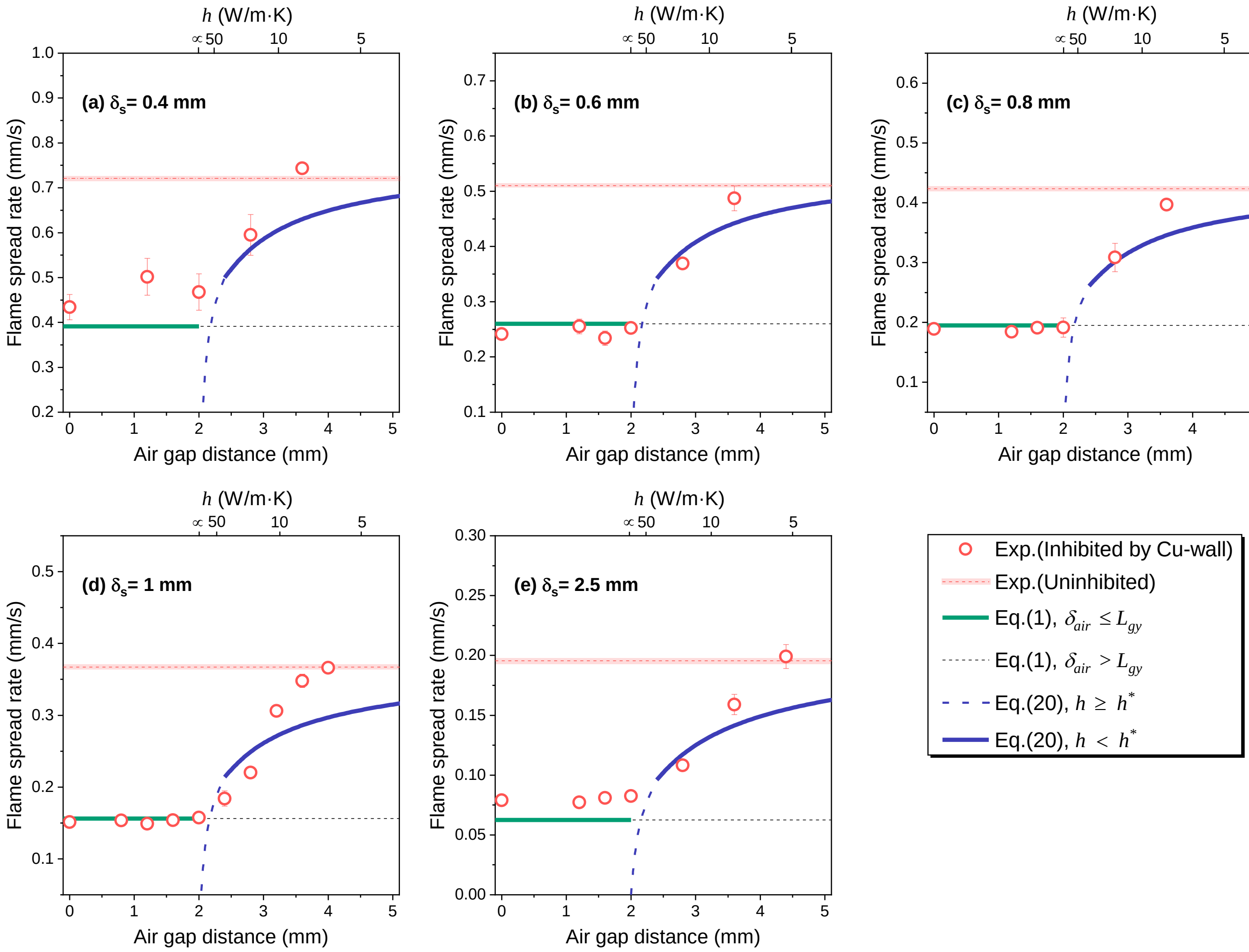

Fig. 12. Experimental results for flame spread rate along sample edge and theoretical prediction from Eq. (20) with $V_{g,eff}$=4.2 cm/s, L_{gy}=2 mm, and Nu=0.24.

Meanwhile, the calculation results of new model are somehow lower than the experimental results at relatively large δ_{air}. This may be attributed from that the present analysis begins with the assumption of constant $V_{g,eff}$ (4.2 cm/s) and L_{gy} (2 mm). $V_{g,eff}$ imposed to the flame front is induced by gravity acting upon the entire flame, and thus the buoyant velocity is affected by the flame size [15, 49]. As shown in Fig. 4, a larger δ_{air} results in a larger surface area of burning zone and hence a larger flame. Therefore, $V_{g,eff}$ is expected to increase with δ_{air}. The overestimation of flow residence time ($t_{g,res} = \alpha_g / V_{g,eff}^2$), flame standoff distance, and corresponding wall heat loss, are the potential cause of this deviation. Furthermore, for some cases, the experimental flame spread rates are slightly larger than the uninhibited one at large air gap distance. It could be explained that the cooling effect from the side wall becomes negligible, but the effective flow velocity imposed to the flame front is still accelerated by the restriction of side wall. Therefore, to incorporate the flow field effect into the closed form flame spread expression is an important further work.

5. Conclusions

Experimental study was conducted on downward flame spread along edge of thin PMMA sheets with the inhibition of metal wall. The effects of sample thickness, wall material, and air gap distance between the side surface of sample and wall (δ_{air}) were investigated theoretically. Major findings include:

(1) Due to the presence of edge flames, there is a transition from conventional two-dimensional flame spread to three-dimensional flame spread as δ_{air} increases. When edge flames appear on the side surface of the sample, FSR at edge achieves steady state immediately after ignition, while the FSR at centerline of the sample begins out slower before accelerating, and eventually catching up to the FSR at edge in the developed stage.

(2) With an increase in δ_{air}, FSR shows three typical regimes: when δ_{air} is small, FSR is consistent to the 2-D FSR, and the edge flame is quenched by the side wall. As δ_{air} exceeds a critical value, the appearance of edge flame results in a significant increase in FSR. The

critical δ_{air} for the onset of edge flame is around 2 mm, regardless of the sample thickness. As δ_{air} is larger than 4 mm, FSR becomes less sensitive to the change of δ_{air}.

(3) FSRs are independent to the wall material because of the large heat capacity of 4 mm-thick metal plate. When the flame spread becomes three-dimensional due to the appearance of edge flame, the heated solid volume is simultaneously determined by the heat penetration depth in the direction of sample thickness and width. The thermally-thin assumption no longer works when air gap distance increases because residence time of flame over solid phase decreases (larger FSR).

(4) The effect of δ_{air} is summarized into two correction factors, one of which describes the enhancement of heat flux from the flame to the solid surface and reduction in heated solid volume caused by surface curvature, and the other of which is an effective flame temperature due to considerable wall heat loss. Based on the heat balance of solid phase in preheating zone and these two correction factors, a modified flame spread model is developed. The well reproduction of FSR further confirms the validity of the theory.

Appendix A. Comparison of the luma tracking and the manual tracking

Figure A1 compares the flame front location extracted from Flame tracker and manual tracking. As seen in Fig. A1 (a), the flame front location was determined automatically using Flame Tracker's luma tracking approach, which is based on intensity thresholds for each pixel. Figure A1 (b) illustrates how to manually characterize the flame front using program created in MATLAB. The typical time evolution of flame front position at right edge of the sample extracted from Flame tracker and

MATLAB is shown in Fig. A1 (c). It can be seen that the flame front position from manual tracking has reasonably good linear growth over time, whereas that using Flame Tracker exhibits some fluctuations (noise) as a result of the intermittent change of brightness of flame front. However, the average flame spread rates obtained from these two method is very close, thus it is believed that Flame tracker can process the original data precisely and quickly.

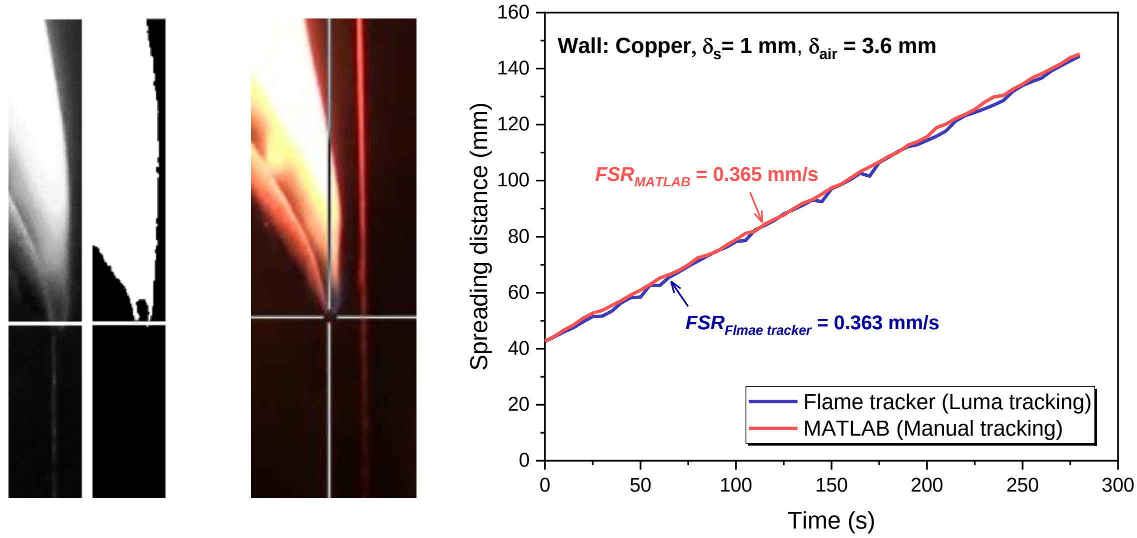

(a) Flame tracker **(b) MATLAB** **(c) Flame front at right edge of the sample**

Fig. A1. Comparison of the flame front location extracted from Flame Tracker (Luma tracking) and MATLAB (Manual tracking).

Appendix B. Wall temperature

Figure B1 shows the representative results of temperature measurement of side wall. Three K-type thermocouples (diameter: 0.3 mm) were installed at the edges of side wall to measure the surface temperature during the flame spread process, as shown in Fig. B1 (a). The temperature history was recorded by a data logger with a sampling rate of 10 Hz. As shown in Fig. B1 (b) and (c), the temperature only increased around 5 K for Cu walls at the time when flame front pass over the thermocouples, whereas it increases around 15 K for SS walls. However, the temperature of side walls will be rapidly increased by the oscillation of downstream flame, especially for SS walls.

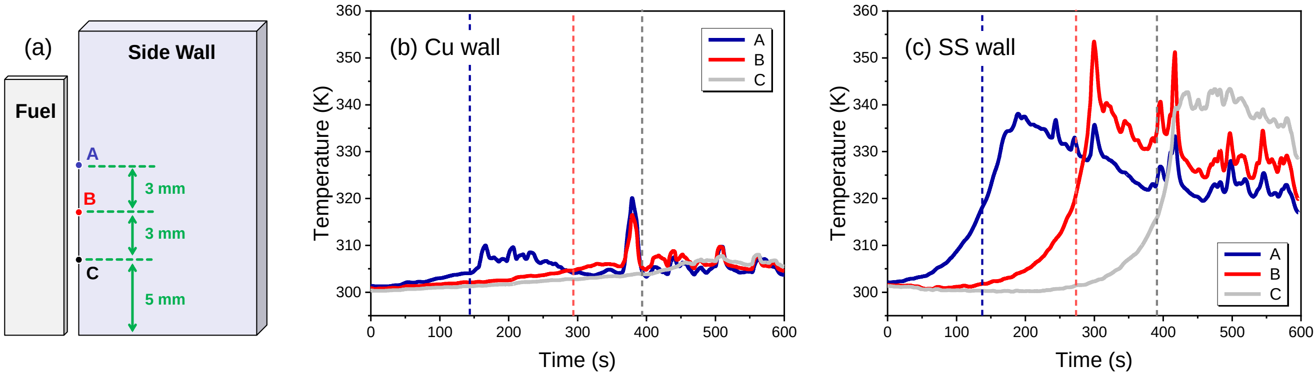

Fig. B1. Temperature measurement of side wall. (a) A schematic of point of measurement, and the typical results of 0.8 mm - thick samples inhibited by (b) Cu wall and (c) SS wall with δ_{air} of 1.6 mm. The dashed line denotes the time when flame front passed over measuring point.

Acknowledgements

This work is carried out as a part of FLARE-2 project (Evaluation of Flammability of Solid Material in Space Habitation) promoted by Japan Space Exploration Agency and supported jointly by JSPS KAKENHI grant number JP21K20389, 22F21343, National Nature Science Foundation of China (No. 52225605) and Chinese Academy of Sciences (No. 211134KYSB20200010 and ZDBS-ZRKJZ-TLC012). The assistance in experiments from Dr. Feng Guo and Ryohei Kojima (Hokkaido Univ.) are acknowledged.

References

[1] O. Fujita, Solid combustion research in microgravity as a basis of fire safety in space, Proc. Combust. Inst. 35 (2015) 2487-2502.

[2] Y. Konno, Y. Li, J.M. Citerne, G. Legros, A. Guibaud, N. Hashimoto, O. Fujita, Experimental study on downward/opposed flame spread and extinction over electric wires in partial gravity environments, Proc. Combust. Inst., doi:10.1016/j.proci.2022.07.002.

[3] NASA STD 6001B. Administration, Flammability, Offgassing, and Compatibility Requirements and Test Procedures, 2011.
[4] I. 4589-2, Plastic – Determination of Burning Behaviour by Oxygen Index – Part2: Ambient – Temperature Test, 2017.
[5] F. Laoutid, L. Bonnaud, M. Alexandre, J.-M. Lopez-Cuesta, P. Dubois, New prospects in flame retardant polymer materials: From fundamentals to nanocomposites, Mater. Sci. Eng. R Rep. 63 (2009) 100-125.
[6] A. Shrivastava, Introduction to Plastics Engineering, William Andrew Publishing: New York, NY, USA, 2018.
[7] G.H. Harkstein, J. de Ris, Flame spread along fuel edges, J. Fire Flammabl. 6 (1975) 140-154.
[8] J. Gong, X. Zhou, J. Li, L. Yang, Effect of finite dimension on downward flame spread over PMMA slabs: Experimental and theoretical study, Int. J. Heat Mass Transf. 91 (2015) 225-234.
[9] K. Zhao, X. Zhou, X. Liu, W. Tang, M.J. Gollner, F. Peng, L. Yang, Experimental and theoretical study on downward flame spread over uninhibited PMMA slabs under different pressure environments, Appl. Therm. Eng. 136 (2018) 1-8.
[10] Y. Wang, J. Zhang, Influences of specimen size and heating mode on the ignitability of polymeric materials in typical small-scale fire test conditions, Fire Mater. 36 (2012) 231-240.
[11] Y. Wang, J. Jow, K. Su, J. Zhang, Development of the unsteady upward fire model to simulate polymer burning under UL94 vertical test conditions, Fire Saf. J. 54 (2012) 1-13.
[12] C.G. McCoy, S.I. Stoliarov, Experimental characterization and modeling of boundary conditions and flame spread dynamics observed in the UL-94V test, Combust. Flame 225 (2021) 214-227.
[13] O. Korobeinichev, S.A. Trubachev, A.K. Joshi, A. Kumar, A.A. Paletsky, A.G. Tereshchenko, A.G. Shmakov, R.K. Glaznev, V. Raghavan, A.M. Mebel, Experimental and numerical studies of downward flame spread over PMMA with and without addition of tri phenyl phosphate, Proc. Combust. Inst. 38 (2021) 4867-4875.
[14] T. Delzeit, L. Carmignani, T. Matsuoka, S. Bhattacharjee, Influence of edge propagation on downward flame spread over three-dimensional PMMA samples, Proc. Combust. Inst. 37 (2019) 3203-3209.
[15] T. Matsuoka, Y. Chiba, S. Okuno, H. Torikai, S. Bhattacharjee, T. Yamazaki, Y. Nakamura, Opposed flame spread over folded PMMA plate with various internal angles, Proc. Combust. Inst.,

doi:10.1016/j.proci.2022.07.153.
[16] C. Kumar, A. Kumar, A Computational Study on Opposed Flow Flame Spread Over Thin Solid Fuels with Side-Edge Burning, Combust. Sci. Technol. 182 (2010) 1321–1340.
[17] B. Comas, T. Pujol, Experimental Study of the Effects of Side-Edge Burning in the Downward Flame Spread of Thin Solid Fuels, Combust. Sci. Technol. 184 (2012) 489–504.
[18] S. Bhattacharjee, M. Laue, L. Carmignani, P. Ferkul, S. Olson, Opposed-flow flame spread: A comparison of microgravity and normal gravity experiments to establish the thermal regime, Fire Saf. J. 79 (2016) 111-118.
[19] Y. Konno, S. Taguchi, Y. Uchigaki, N. Hashimoto, O. Fujita, Experimental Observation of Downward Flame Spread over Printed Circuit Board: Influence of Gap Distance between Side Surface of Sample and Sample Holder on Flame Spread Rate and Extinction Limit, The Proceedings of the Thermal Engineering Conference, doi:10.1299/jsmeted.2021.0068.
[20] Y. Kobayashi, N. Matsukawa, K. Matsumoto, F. Takahashi, Theoretically predicting the flame-spread limit of carbon-fiber-reinforced plastic, Proc. Combust. Inst., doi:10.1016/j.proci.2022.07.130.
[21] Y. Kobayashi, K. Terashima, R. Oiwa, M. Tokoro, S. Takahashi, Opposed-flow flame spread over carbon fiber reinforced plastic under variable flow velocity and oxygen concentration: The effect of in-plane thermal isotropy and anisotropy, Proc. Combust. Inst. 38 (2021) 4857-4866.
[22] X. Huang, J. Gao, A review of near-limit opposed fire spread, Fire Safety Journal 120 (2020) 103141.
[23] S. Bhattacharjee, K. Wakai, S. Takahashi, Predictions of a critical fuel thickness for flame extinction in a quiescent microgravity environment, Combust. Flame 132 (2003) 523-532.
[24] S. Takahashi, H. Ito, Y. Nakamura, O. Fujita, Extinction limits of spreading flames over wires in microgravity, Combust. Flame 160 (2013) 1900-1902.
[25] Y. Konno, N. Hashimoto, O. Fujita, Role of wire core in extinction of opposed flame spread over thin electric wires, Combust. Flame 220 (2020) 7-15.
[26] Y. Ma, X. Zhang, Y. Lu, J. Lv, N. Zhu, L. Hu, Effect of transverse flow on flame spread and extinction over polyethylene-insulated wires, Proc. Combust. Inst. 38 (2021) 4727-4735.
[27] S. Jia, L. Hu, Y. Ma, X. Zhang, O. Fujita, Experimental study of downward flame spread and extinction over inclined electrical wire under horizontal wind, Combust. Flame 237 (2022) 111820.
[28] S. Lin, H. Yuan, X. Huang, A computational study on the quenching and near-limit propagation

of smoldering combustion, Combust. Flame 238 (2022) 111937.
[29] S. Lin, X. Huang, Quenching of smoldering: Effect of wall cooling on extinction, Proc. Combust. Inst. 38 (2021) 5015-5022.
[30] S. Bhattacharjee, R. Altenkirch, The effect of surface radiation on flame spread in a quiescent, microgravity environment, Combust. Flame 84 (1991) 160-169.
[31] C. Kumar, A. Kumar, On the role of radiation and dimensionality in predicting flow opposed flame spread over thin fuels, Combust. Theory Model. 16 (2012) 537-569.
[32] F. Takahashi, M. Kondou, K. Waikai, S. Bhattacharjee, Effect of radiation loss on flame spread over a thin PMMA sheet in microgravity, Proc. Combust. Inst. 29 (2002) 2579-2586.
[33] S. Bhattacharjee, R. Ayala, K. Wakai, S. Takahashi, Opposed-flow flame spread in microgravity-theoretical prediction of spread rate and flammability map, Proc. Combust. Inst. 30 (2005) 2279-2286.
[34] S. Takahashi, M.A.F. Borhan, K. Terashima, A. Hosogai, Y. Kobayashi, Flammability limit of thin flame retardant materials in microgravity environments, Proc. Combust. Inst. 37 (2019) 4257–4265.
[35] S. Bhattacharjee, L. Carmignani, Radiation-kinetics interactions: A comparison of opposed-flow flame spread in a low-velocity microgravity and low-pressure downward environments, Proc. Combust. Inst. 38 (2021) 4795-4803.
[36] J.G. Quintiere, Fundamentals of Fire Phenomena, John Wiley & Sons, New York, 2006.
[37] Y. Kobayashi, Y. Konno, X. Huang, S. Nakaya, M. Tsue, N. Hashimoto, O. Fujita, A.C. Fernandez-Pello, Effect of insulation melting and dripping on opposed flame spread over laboratory simulated electrical wires, Fire Saf. J. 95 (2018) 1-10.
[38] S. Bhattacharjee, R. Nagarkar, Y. Nakamura, A Correlation for an Effective Flow Velocity for Capturing the Boundary Layer Effect in Opposed-Flow Flame Spread over Thin Fuels, Combust. Sci. Technol. 186 (2014) 975-987.
[39] L. Carmignani, Flame Tracker: An image analysis program to measure flame characteristic, SoftwareX 15 (2021) 100791.
[40] O. Fujita, K. Nishizawa, K. Ito, Effect of low external flow on flame spread over polyethylene-insulated wire in microgravity, Proc. Combust. Inst. 22 (2002) 2545–2552.
[41] M.A. Delichatsios, Exact Solution for the Rate of Creeping Flame Spread over Thermally Thin Materials, Combust. Sci. Technol. 44 (1984) 257-267.
[42] M.A. Delichatsios, Effects of material thickness on ignition times and creeping flame spread in

the thermal regime: Theory, analytical solution and experimental justification, Fire Saf. J. 116 (2020) 103204.

[43] S. Bhattacharjee, T. Delzeit, Opposed-flow flame spread over cylindrical fuels: Spread rate formulas and experimental, Proc. Combust. Inst., doi:10.1016/j.proci.2022.07.243.

[44] M.A. Delichatsios, R.A. Altenkirch, M. Bundy, S. Bhattacharjee, L. Tang, K. Sacksteder, Creeping flame spread along fuel cylinders in forced and natural flows and microgravity, Proc. Combust. Inst. 28 (2000) 2835-2842.

[45] S. Olson, F. Miller, S. Jahangirian, I.S. Wichman, Flame spread over thin fuels in actual and simulated microgravity conditions, Combust. Flame 156 (2009) 1214-1226.

[46] L. Zhao, J. Fang, X. He, J. Wang, S. Tao, Y. Zhang, An analysis of width effects on flame spread in conjunction with concurrent forced flow using a variable B-number, Combust. Flame 194 (2018) 334-342.

[47] K. Zhao, X. Zhou, L. Yang, J. Gong, Z. Wu, Z. Huan, X. Liu, Width effects on downward flame spread over poly(methyl methacrylate) sheets, J. Fire Sci. 33 (2015) 69-84.

[48] K. Seshadri, F.A. Williams, Structure and extinction of counterflow diffusion flames above condensed fuels: Comparison between poly(methyl methacrylate) and its liquid monomer, both burning in nitrogen–air mixtures, J. Polymer Sci. . A: Polymer Chem. 167 (1978) 1755-1778.

[49] M.C. Johnston, J.S. T'ien, D.E. Muff, X. Zhao, S.L. Olson, P.V. Ferkul, Self induced buoyant blow off in upward flame spread on thin solid fuels, Fire Saf. J. 71 (2015) 279-286.